Monthly Notices of the ROYAL ASTRONOMICAL SOCIETY
MNRAS Advance Access published October 29, 2012
MNRAS (2012) doi:10.1093/mnras/sts119

Clustering, bias and the accretion mode of X-ray-selected AGN

L. Koutoulidis,[1,2] M. Plionis,[3,4⋆] I. Georgantopoulos[1,5] and N. Fanidakis[6]

[1]*National Observatory of Athens, V. Paulou & I. Metaxa 11532, Greece*
[2]*Physics Department, University of Patras, Patras, Greece*
[3]*Department of Physics, Aristotle University of Thessaloniki, Thessaloniki 54124, Greece*
[4]*Instituto Nacional de Astrofísica, Óptica y Electrónica, L.Enrique Erro 1, Tonantzintla, Puebla, CP 72840, Mexico*
[5]*INAF – Osservatorio Astronomico di Bologna, Via Ranzani 1, I-40127 Bologna, Italy*
[6]*Max Planck Institute for Astronomy, Königstuhl 17 D-69117, Heidelberg, Germany*

Accepted 2012 October 1. Received 2012 October 1; in original form 2012 July 18

ABSTRACT

We present the spatial clustering properties of 1466 X-ray-selected active galactic nuclei (AGN) compiled from the *Chandra* Deep Field (CDF) North and South, extended CDF-S, COSMOS and All-wavelength Extended Groth strip International Survey (AEGIS) fields in the 0.5–8 keV band. The X-ray sources span the redshift interval $0 < z < 3$ and have a median value of $\bar{z} = 0.976$. We employ the projected two-point correlation function to infer the spatial clustering and find a clustering length of $r_0 = 7.2 \pm 0.6\,h^{-1}$ Mpc and a slope of $\gamma = 1.48 \pm 0.12$, which corresponds to a bias of $b(\bar{z}) = 2.26 \pm 0.16$. Using two different halo bias models, we consistently estimate an average dark-matter host halo mass of $M_{\rm h} \simeq 1.3(\pm 0.3) \times 10^{13}\,h^{-1}\,{\rm M}_{\odot}$. The X-ray AGN bias and the corresponding dark-matter host halo mass are significantly higher than the corresponding values of optically selected AGN (at the same redshifts). The redshift evolution of the X-ray-selected AGN bias indicates, in agreement with other recent studies, that a unique dark-matter halo mass does not fit well the bias at all the different redshifts probed. Furthermore, we investigate if there is a dependence of the clustering strength on X-ray luminosity. To this end we consider only 650 sources around $z \sim 1$ and we apply a procedure to disentangle the dependence of clustering on redshift. We find indications for a positive dependence of the clustering length on X-ray luminosity, in the sense that the more luminous sources have a larger clustering length and hence a higher dark-matter halo mass. In detail we find for an average luminosity difference of $\delta \log_{10} L_x \simeq 1$ a halo mass difference of a factor of $\sim$3.

These findings appear to be consistent with a galaxy formation model where the gas accreted on to the supermassive black hole in intermediate-luminosity AGN comes mostly from the hot-halo atmosphere around the host galaxy.

Key words: galaxies: active – X-rays: galaxies – large scale structure of Universe – dark matter.

1 INTRODUCTION

One of the most remarkable astronomical findings of the last decade is the discovery of the scaling relations between the mass of supermassive black holes (BHs) and the properties of the large-scale environment of their host galaxies. In particular, observations suggest that there is a tight correlation between the BH mass and the bulge velocity dispersion, stellar mass and luminosity of the spheroidal component of the host galaxy (e.g. Magorrian et al. 1998; Häring & Rix 2004; Ferrarese & Ford 2005; Gültekin et al. 2009). These observational relations indicate that the cosmic growth of BH mass is strongly coupled to the evolution of the host spheroid. However, the physical mechanism that shapes these relations is still unknown.

In most semi-analytic models of galaxy formation (e.g. Bower et al. 2006; Croton et al. 2006; Lagos, Cora & Padilla 2008; Somerville et al. 2008) it is assumed that the active galactic nucleus (AGN) associated with accreting BH regulates the formation of new stars. The mechanisms adopted by semi-analytical models for triggering AGN activity include major galaxy mergers for the most luminous AGN (Di Matteo, Springel & Hernquist 2005; Hopkins et al. 2006; Marulli et al. 2009), while it is possible that in the lowest luminosity AGN regime secular disc instabilities or minor interactions play the key role (Hopkins & Hernquist 2006; Bournaud et al. 2011). These different AGN fuelling modes make diverse predictions for the environment of the galaxies that host AGN (Shankar, Weinberg & Miralda-Escudé 2009). For example, in the major-merger scenario, only weak luminosity dependence on clustering is expected (Hopkins et al. 2005; Lidz et al. 2006;

⋆ E-mail: mplionis@astro.noa.gr

Bonoli et al. 2009). Hence, observational studies of AGN clustering and its dependence on luminosity can place valuable constraints on the AGN fuelling modes and consequently on the AGN–galaxy co-evolution models.

The clustering of AGN has been studied with excellent statistics mainly in the optical and particularly in large area surveys, such as the 2QZ (Two-degree Field [2dF] QSO Redshift Survey; Croom et al. 2005; Porciani & Norberg 2006) and the SDSS (Sloan Digital Sky Survey; Li et al. 2006; Ross et al. 2009; Shen et al. 2009). These surveys found no evidence for a strong dependence of clustering on luminosity (e.g. Croom et al. 2005; Myers et al. 2006; da Ângela et al. 2008) although Shen et al. (2009) detect an excess of clustering for their 10 per cent brightest quasars. However, optical QSO may represent only the tip of the iceberg of the AGN population. Very deep X-ray surveys find a surface density of about 10 000 deg^{-2} (Xue et al. 2011), which is about two orders of magnitude higher than that found in optical QSO surveys (Wolf et al. 2003). Several studies have explored the angular clustering of AGN in X-ray wavelengths (Vikhlinin & Forman 1995; Akylas, Georgantopoulos & Plionis 2000; Yang et al. 2003; Basilakos et al. 2004, 2005; Gandhi et al. 2006; Puccetti et al. 2006; Carrera et al. 2007; Miyaji et al. 2007; Plionis et al. 2008; Ebrero et al. 2009; Bradshaw et al. 2011; Elyiv et al. 2012). These studies measure the projected angular clustering and then via Limber's equation (Peebles 1980) derive the corresponding spatial clustering length. However, in this method a priori knowledge of the redshift distribution dN/dz is needed, and thus the uncertainties may be appreciable.

Recently, several studies have attempted to measure the spatial correlation function of X-ray-selected AGN by employing spectroscopic redshifts to estimate their correct distances (Mullis et al. 2004; Gilli et al. 2005, 2009; Yang et al. 2006; Coil et al. 2009; Hickox et al. 2009; Cappelluti et al. 2010; Krumpe, Miyaji & Coil 2010; Allevato et al. 2011; Miyaji et al. 2011; Starikova et al. 2011). These studies show that X-ray are typically hosted in DM haloes with mass of the order of $12.5 < \log_{10}(M_{\rm h}/[h^{-1}\,{\rm M}_{\odot}]) < 13.5$, at a redshift of $z \sim 1$. On the issue of luminosity-dependent clustering the results are contentious. Yang et al. (2006) did not detect strong correlation between X-ray luminosity and the clustering amplitude for *Chandra* sources. Gilli et al. (2009) performed a similar investigation in the *XMM*–COSMOS field dividing the sample below and above $L_{\rm x}(0.5\text{–}10\,{\rm keV}) = 10^{44}\,{\rm erg\,s^{-1}}$ and did not find any luminosity dependence. Similarly, Starikova et al. (2011), using 1282 *Chandra*/Bootes sources, did not find a significant dependence of clustering on luminosity.

On the other hand, Plionis et al. (2008) first reported strong indications for luminosity-dependent clustering of X-ray AGN in the CDF fields for both soft and hard bands in the sense that X-ray luminous AGN lie in more massive dark-matter (DM) haloes compared to the less luminous ones. Coil et al. (2009) using AGN in the redshift range $z = 0.7\text{–}1.4$ from the AEGIS field found weak evidence for luminosity-dependent clustering, but not at a statistically significant level. In addition, Krumpe et al. (2010) using low-redshift ($z \sim 0.25$) AGN, selected from the *ROSAT* All-Sky Survey and cross-matched with the SDSS, found that $L_{\rm x} > 10^{44}\,{\rm erg\,s^{-1}}$ sources are clustered more strongly than lower luminosity sources. In another recent study, Cappelluti et al. (2010) using a sample of 199 *Swift*- BAT sources in the 15–55 keV band found marginally significant luminosity-dependent clustering.

In this paper we use a sample of 1466 sources selected in the 0.5–8 keV band from a variety of deep *Chandra* X-ray surveys to estimate the spatial correlation function and typical DM host halo mass of X-ray-selected AGN. Our aim is to investigate whether there is a luminosity dependence on clustering, and also to obtain insight into the BH fuelling mechanisms, using the largest X-ray-selected AGN sample used so far for this scope. The paper is organized as follows. In Section 2, we briefly discuss the X-ray surveys we consider in this paper and in Section 3, we describe the methodology of our clustering analysis. In Section 4, we present our findings for the AGN correlation function as estimated by the joint and individual X-ray samples. In Section 5, we calculate the bias of AGN and its redshift evolution, and estimate the average mass of the DM haloes hosting X-ray AGN. In Section 6, we investigate the dependence of the halo mass on X-ray luminosity and compare our findings with theoretical galaxy formation models for the evolution of accreting BHs. Finally, we present in Section 7 our conclusions. For comparison reasons with previous works we adopt, unless otherwise stated, a flat cosmology with a present-day matter density parameter $\Omega_{\rm m} = 0.3$, a cosmological constant $\Omega_{\Lambda} = 0.7$ and the baryon density $\Omega_{\rm b} = 0.04$. The Hubble constant is expressed in units of h as $H_0 = 100\,h$ km s^{-1} Mpc $^{-1}$.

2 AGN CATALOGUES

We make use of X-ray data coming from the five deepest X-ray surveys, namely the *Chandra* Deep Field South and North (CDF-S and CDF-N), the AEGIS, the extended *Chandra* Deep Field South (ECDF-S) and the COSMOS. These cover a variety of exposures (from 4 Ms down to 40 ks) and surveyed area, and thus cover extensively the luminosity–redshift space. Moreover, these fields contain excellent quality spectroscopic observations and therefore good quality redshifts, which are essential in this project. Below we present briefly the main characteristics of the X-ray surveys used in this work.

2.1 Chandra deep field north

The deep pencil-beam CDF-N survey covers an area of 448 arcmin^2, is centred at $\alpha = 12^{\rm h}36^{\rm m}49^{\rm s}, \delta = +62^{\circ}12'58''$ and consists of 20 individual ACIS-I (Advanced CCD Imaging Spectrometer) pointings. The combined observations provide the deepest X-ray sample currently available together with the CDF-S. Here, we use the X-ray 2 Ms source catalogue of Alexander et al. (2003), with a sensitivity of $\sim 10^{-17}$ erg cm^{-2} s^{-1}, which consists of 503 sources in the 0.5–8 keV band. Spectroscopic redshifts were used for 243 X-ray sources in the redshift interval $z = 0\text{–}3$ from Trouille et al. (2008, and references therein).

2.2 Chandra deep field south

The deep pencil-beam CDF-S survey covers an area of 436 arcmin^2 and the average aim point is $\alpha = 03^{\rm h}32^{\rm m}28\overset{\rm s}{.}8$, $\delta = -27^{\circ}48'23''$(J2000). The analysis of all 23 observations is presented in Luo et al. (2008). We use the 2 Ms X-ray source catalogue of Luo et al. (2008), which consists of 462 X-ray sources. Spectroscopic redshifts were used for 219 X-ray sources in the redshift interval $z = 0\text{–}3$ from Luo et al. (2010).

2.3 AEGIS

The ultra-deep field survey comprises pointings at eight separate positions, each with a nominal exposure of 200 ks, covering a total area of approximately 0.67 deg^2 centred at $\alpha = 14^{\rm h}17^{\rm m}, \delta = +52^{\circ}30'$ in a strip of length of 2°. The flux limit of the survey is $S \sim 10^{-16}$ erg s^{-1} cm^{-2} in the full band. We use the X-ray source

catalogue of Laird et al. (2009), which consists of 1325 sources. Spectroscopic redshifts were used for 392 X-ray sources in the redshift interval $z = 0$–3 from DEEP2 (Davis et al. 2001, 2003; Coil et al. 2009).

2.4 COSMOS

The *Chandra* COSMOS Survey covers the central 0.5 deg^2 area of the COSMOS field with an effective exposure of ∼160 ks and the rest of the field with an effective exposure of ∼80 ks. The limiting source detection depths are 5.7×10^{-16} erg s^{-1} cm^{-2} in the full band. We use the source catalogue of Elvis et al. (2009), which consists of 1761 sources. Spectroscopic redshifts were used for 417 X-ray sources from Brusa et al. (2010).

2.5 Extended Chandra deep field south

The ECDF-S survey consists of four *Chandra* 250 ks ACIS-I pointings covering ∼0.3 deg^2 and surrounding the original CDF-S. Source detection has been performed by Lehmer et al. (2005) and Virani et al. (2006). Here we use the source detection of Lehmer et al. (2005) in which 762 sources have been detected. The flux limit of ECDF-S is $S \sim 10^{-16}$ erg s^{-1}cm^{-2}. Spectroscopic redshifts were used for 288 sources in the redshift interval $z = 0-3$ from Silverman et al. (2010). When combining all fields, we exclude sources that are detected both in ECDF-S and CDF-S, and keep only those detected in the ECDF-S.

3 METHODOLOGY

3.1 Theoretical considerations

The main statistic used to measure the clustering of extragalactic sources is the two-point correlation function $\xi(r)$. $\xi(r)$ describes the excess probability over random of finding a pair with one object in an elemental volume $\mathrm{d}V_1$ and the second in the elemental volume $\mathrm{d}V_2$, separated by a distance r (e.g. Peebles 1980). Its mathematical description is given by $\mathrm{d}P = \langle n \rangle^2 [1 + \xi(s)] \mathrm{d}V_1 \mathrm{d}V_2$, where $\langle n \rangle$ is the mean space density of the sources under study and $s = cz$. When measuring ξ directly from redshift catalogues of sources, we include the distorting effect of peculiar velocities, since the true distance of a source is $r = (s - \boldsymbol{v}_p \cdot \boldsymbol{r})/H_0$, where $\boldsymbol{v}_p \cdot \boldsymbol{r}$ is the component of the peculiar velocity of the source along the line of sight. In order to avoid such effects one can measure the angular clustering, which is not hampered by the effects of z-distortions, and then, under some assumptions, infer the spatial correlation function through Limber's integral equation (Limber 1953). Alternatively, one can use the redshift information to measure the so-called projected correlation function, $w_\mathrm{p}(r_\mathrm{p})$ (e.g. Davis & Peebles 1983), and then infer the spatial clustering.

To this end, one deconvolves the redshift-based distance of a source, s, in two components, one parallel (π) and one perpendicular (r_p) to the line of sight, i.e. $s = (r_\mathrm{p}^2 + \pi^2)^{1/2}$, and thus the redshift-space correlation function can be written as $\xi(s) = \xi(r_\mathrm{p}, \pi)$. Since redshift-space distortions affect only the π component, one can estimate the projected correlation function, $w_\mathrm{p}(r_\mathrm{p})$, free of z-space distortions by integrating $\xi(r_\mathrm{p}, \pi)$ along π:

$$w_\mathrm{p}(r_\mathrm{p}) = 2 \int_0^\infty \xi(r_\mathrm{p}, \pi) \mathrm{d}\pi. \quad (1)$$

Once we estimate the projected correlation function, $w_\mathrm{p}(r_\mathrm{p})$, we can recover the real-space correlation function, since the two are related according to (Davis & Peebles 1983)

$$w_\mathrm{p}(r_\mathrm{p}) = 2 \int_0^\infty \xi\left(\sqrt{r_\mathrm{p}^2 + \pi^2}\right) \mathrm{d}\pi = 2 \int_{r_\mathrm{p}}^\infty \frac{r \xi(r) \mathrm{d}r}{\sqrt{r^2 - r_\mathrm{p}^2}}. \quad (2)$$

Modelling $\xi(r)$ as a power law, $\xi(r) = (r/r_0)^{-\gamma}$, one obtains

$$w_\mathrm{p}(r_\mathrm{p}) = A_\gamma r_\mathrm{p} \left(\frac{r_0}{r_\mathrm{p}}\right)^\gamma, \quad (3)$$

with

$$A\gamma = \Gamma\left(\frac{1}{2}\right) \Gamma\left(\frac{\gamma - 1}{2}\right) / \Gamma\left(\frac{\gamma}{2}\right), \quad (4)$$

where Γ is the usual gamma function.

However, it should be noted that although equation (3) strictly holds for $\pi_\mathrm{max} = \infty$, practically we always impose a cutoff π_max (for reasons discussed in the next subsection). This introduces an underestimation of the underlying correlation function, which is an increasing function of separation r_p. For a power-law correlation function this underestimation is easily inferred from equation (2) and is given by (e.g. Starikova et al. 2011)

$$C_\gamma(r_\mathrm{p}) = \frac{\int_0^{\pi_\mathrm{max}} (r^2 - \pi^2)^{-\gamma/2} \mathrm{d}\pi}{\int_0^\infty (r^2 - \pi^2)^{-\gamma/2} \mathrm{d}\pi}. \quad (5)$$

Thus, by taking into account the above statistical correction, and under the assumption of the power-law correlation function, one can recover the corrected spatial correlation function, $\xi(r_\mathrm{p})$, from the fit to the measured $w_\mathrm{p}(r_\mathrm{p})$ according to (which also provides the value of γ)

$$\xi(r_\mathrm{p}) = \frac{1}{A_\gamma C_\gamma(r_\mathrm{p})} \frac{w_\mathrm{p}(r_\mathrm{p})}{r_\mathrm{p}}. \quad (6)$$

However, at large separations the correction factor increasingly dominates over the signal and thus it constitutes the correction procedure unreliable. Alternatively, as can be easily shown using equations (3) and (6), a crude estimate of the corrected spatial correlation length can be provided by

$$r_{0,\mathrm{c}} = r_0 C_\gamma(r_0)^{-1/\gamma}, \quad (7)$$

where r_0 and γ are derived from fitting the data to equation (3).

3.2 Correlation function estimator

As a first step we calculate $\xi(r_\mathrm{p}, \pi)$ using the estimator (cf. Kerscher, Szapudi & Szalay 2000)

$$\xi(r_\mathrm{p}, \pi) = \frac{N_\mathrm{R}}{N_\mathrm{D}} \frac{DD(r_\mathrm{p}, \pi)}{DR(r_\mathrm{p}, \pi)}, \quad (8)$$

where N_D and N_R are the number of data and random sources, respectively, while $DD(r_\mathrm{p}, \pi)$ and $DR(r_\mathrm{p}, \pi)$ are the number of data–data and data–random pairs, respectively. We then estimate the redshift-space correlation function, $\xi(s)$, in the range $s = 0.16-40\,h^{-1}$ Mpc and the projected correlation function, $w_\mathrm{p}(r_\mathrm{p})$, in the separation range $r_\mathrm{p} = 0.16-20\,h^{-1}$ Mpc. Note that large separations in the π direction add mostly noise to the above estimator and therefore the integration is truncated for separations larger than π_max. The choice of π_max is a compromise between having an optimal signal-to-noise ratio for ξ and reducing the excess noise from

high-π separations. The majority of studies in the literature usually assume $\pi_{\rm max} \in [5, 30]\,h^{-1}$ Mpc.

The correlation function uncertainty is estimated according to

$$\sigma_{w_{\rm p}} = \sqrt{3}(1 + w_{\rm p})/\sqrt{DD}, \quad (9)$$

which corresponds to that expected by the bootstrap technique (Mo, Jing & Boerner 1992). In this work, we bin the source pairs in logarithmic intervals of $\delta \log_{10}(r_{\rm p}, \pi) = 0.15$ and $\delta \log_{10}(s) = 0.17$ for the $w_{\rm p}(r_{\rm p})$ and $\xi(s)$ correlation functions, respectively. Finally, we use a χ^2 minimization procedure between data and the power-law model for either type of the correlation function to derive the best-fitting r_0 and γ parameters. We carefully choose the range of separations in order to obtain the best power-law fit to the data and we impose a lower separation limit of $r_{\rm p} \sim 1.5\,h^{-1}$ Mpc to minimize non-linear effects.

3.3 Random catalogue construction

To estimate the spatial correlation function of a sample of sources, one needs to construct a large mock comparison sample with a random spatial distribution within the survey area, which also reproduces all the systematic biases that are present in the source sample (i.e. instrumental biases due to the point spread function variation, vignetting, etc). Also special care has to be taken to reproduce any biases that enter through the optical counterpart spectroscopic observation strategy (cf. due to the positioning of the masks within the field of view and that of the slits within the masks, etc).

To this end we will follow the random catalogue construction procedure of Gilli et al. (2005, hereafter G05), which is based on reshuffling only the source redshifts, smoothing the corresponding redshift distribution, while keeping the angular coordinates unchanged. We will test the efficiency of this method by comparing the correlation function results with those of the standard method that takes into account the details of the sensitivity maps of each *XMM* pointing. We further test the two methods using *N*-body simulations for the underlying DM density field.

3.3.1 *Random redshift reshuffling method*

In order to assign random redshifts to the mock sample, the source redshift distribution is smoothed using a Gaussian kernel with a smoothing length of $\sigma_z = 0.3$. This offers a compromise between scales that are either too small, and thus may reproduce the z-space clustering, or too large and thus oversmooth the observed redshift distribution. We verified that our results do not change significantly when using a smoothing length in the range $\sigma_z = 0.2$–0.4.

3.3.2 *Standard 'sensitivity map' method*

According to the standard method of producing random catalogues, each simulated source is placed at a random position on the sky, with a flux randomly extracted from the observed source $\log N - \log S$ (source number–flux distribution). If the flux is above the value allowed by the sensitivity map at that position, the simulated source is kept in the random sample and a random redshift is also assigned to it from the observed source redshift distribution $N(z)$ (optimally taking into account the variation of $N(z)$ as a function of flux). The disadvantage of this method is that it does not take into account any unknown inhomogeneities and systematics of the follow-up spectroscopic observations.

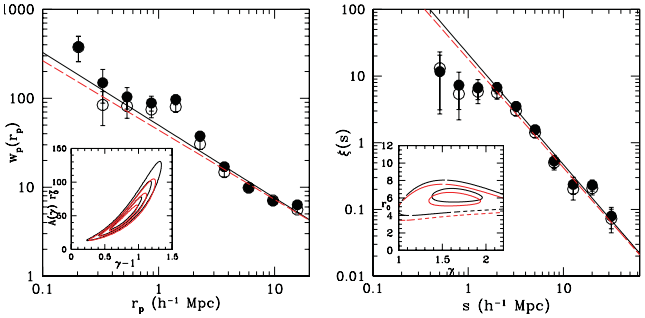

Figure 1. Comparison of the correlation function results based on the G05 random construction method (filled symbols) with that of the standard 'sensitivity map' method (empty symbols), applied on the AEGIS full band (0.5–8 keV) catalogue. Uncertainties correspond to 1σ Poisson errors. The best-fitting power laws are shown as black lines for the G05 method and as dashed red lines for the sensitivity map method. In the inset panels we show the likelihood 1σ, 2σ, 3σ contours in the two-parameter solution space. Right-hand panel: redshift-space correlation function, $\xi(s)$. Left-hand panel: projected correlation function, $w_{\rm p}(r_{\rm p})$.

3.3.3 *Testing the efficiency of the two methods*

In order to test the efficiency of the two random catalogue construction methods we use the AEGIS survey, consisting of eight fields. To construct the standard method random catalogue, we use the sensitivity maps of Laird et al. (2009) and compute the projected and redshift-space two-point correlation functions. The best-fitting correlation length found is $r_0 = 4.28 \pm 0.14\,h^{-1}$ Mpc for $\gamma = 1.8$ which is in excellent agreement with the results based on the G05 method: $r_0 = 4.13 \pm 0.14\,h^{-1}$ Mpc. In Fig. 1, we compare the correlation functions for the two random construction methods.

3.3.4 *A further test using simulations*

We use a 500 h^{-1} Mpc cube simulation of a flat $\Omega_{\rm m} = 0.3$ and $\sigma_8 = 0.9$ cosmology with 512^3 particles (Ragone-Figueroa & Plionis 2007) to further test the robustness of the G05 random sample construction method. In order to have a relatively wide redshift range, we replicate randomly the box to get an effective volume of $1500^3\,h^{-3}$ Mpc^3. To obtain a relatively large but manageable source density, we selected DM haloes with $M_{\rm h} > 1.5 \times 10^{14}\,h^{-1}\,{\rm M}_\odot$, which resulted in a total number of haloes within our large simulation volume of $N = 9 \times 2312$.

We estimate the actual halo correlation function according to the *direct* method, which entails counting the number of DM halo pairs within spherical shells around a given halo. The corresponding number of random pairs is estimated by $\langle n\delta \rangle V$, with $\langle n \rangle$ being the mean number density of haloes in the whole simulation volume and δV the volume of the spherical shell, i.e. $4/3\pi\delta r^3$, with δr being the width of the spherical shell.

We also estimate the halo correlation function using the G05 method, for which we transform the halo Cartesian coordinates into spherical coordinates, determining also their distance distribution. The clustering results of the two methods are in excellent agreement providing $\gamma = 1.72(\pm 0.05)$ and $1.68(\pm 0.12)$ as well as $r_0 = 13.9(\pm 0.3)$ and $13.2(\pm 0.5)\,h^{-1}$ Mpc for the *direct* and G05 correlation function estimations, respectively.

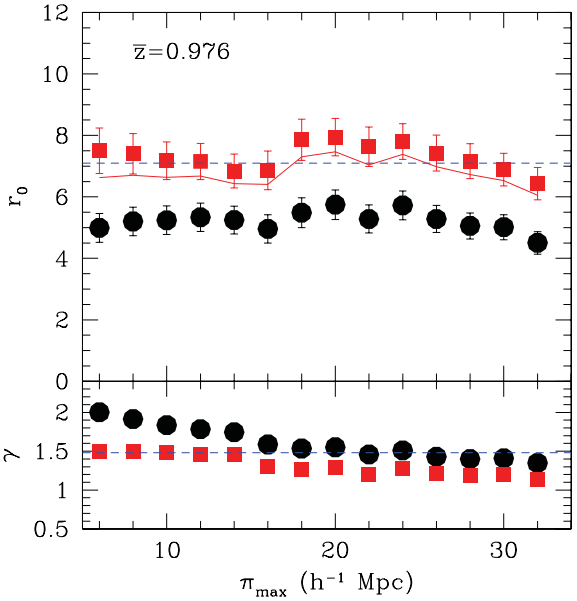

Figure 2. The resulting amplitude r_0, and slope γ, of the correlation function analysis as a function of the value of the $\pi_{\rm max}$ cutoff. The filled circles correspond to the results based on $w_{\rm p}(r_{\rm p})$, while the red squares to the results of $\xi(r_{\rm p})$. The continuous red line corresponds to the crude estimation of the corrected spatial amplitude based on equation (7), while the dashed blue line corresponds to the finally adopted results (which corresponds to the $\pi_{\rm max} = 10\,h^{-1}$ Mpc case).

Table 1. Clustering results for the joint sample of all five fields (1466 sources). The clustering length unit is h^{-1} Mpc. The results correspond to $\pi_{\rm max} = 10\,h^{-1}$ Mpc, but they are very similar over the whole indicated $\pi_{\rm max}$ range, but more so for $5 \lesssim \pi_{\rm max} \lesssim 16\,h^{-1}$ Mpc, as can be seen from Fig. 2. The cosmic variance is estimated to give a further ∼0.3 uncertainty in r_0.

	γ	r_0	r_0 ($\gamma = 1.8$)
$w_{\rm p}(r_{\rm p})$	1.84±0.07	5.2±0.5	5.2 ± 0.5
$\xi(s)$	1.49±0.20	6.6±1.0	6.0 ± 0.8
$\xi(r_{\rm p})$	1.48±0.12	7.2±0.6	6.5 ± 0.4

4 RESULTS

4.1 The joint X-ray sample

Combining all five fields, we obtain in total 1466 X-ray sources with spectroscopic redshifts. The median redshift of the source sample is $\bar{z} = 0.976$. In order to estimate the joint sample correlation function we generate random catalogues for each field separately and then combine them together. Note that we take care to count only once the sources that are common in both the CDF-S and ECDF-S fields.

We remind the reader that we fit a power law to the measured correlation function over a range of separations for which such a model represents well the data. In order to avoid non-linear effects we use a lower separation limit, $r_{\rm p} \simeq 1.5\,h^{-1}$ Mpc, for the fit of s. We also impose an upper separation limit ($\simeq 10\,h^{-1}$ Mpc) since we find a change above this scale in the slope of both projected and z-space correlation functions.

We now investigate the sensitivity of the correlation function on the cutoff separation along the line of sight, $\pi_{\rm max}$, which we vary in the range [5,30]$\,h^{-1}$ Mpc. For $\pi_{\rm max} > 30\,h^{-1}$ Mpc, the

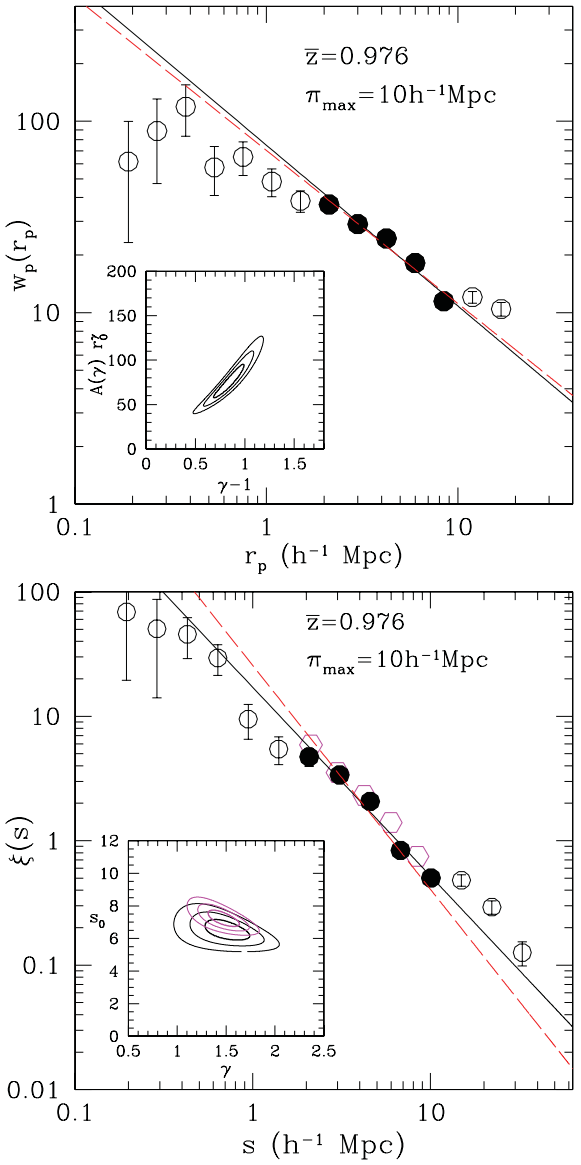

Figure 3. Correlation functions of the joint X-ray point-source sample. The projected correlation function, $w_{\rm p}(r_{\rm p})$, is shown in the upper panel, and the z-space correlation function, $\xi(s)$, is shown in the lower panel. The filled points indicate the range over which a power-law fit was applied (the black line corresponds to a fit with free γ, while the red line to that with $\gamma = 1.8$). The real-space correlation function, $\xi(r_{\rm p})$ (via equation 6), is indicated in the lower panel by magenta pentagons. The inset panels show the 1σ, 2σ and 3σ likelihood contours in the two-parameter plane of the power-law fit solutions.

noise introduced by uncorrelated pairs reduces significantly the correlation function amplitude and slope. In Fig. 2 we show how the amplitude r_0 and the slope γ of the projected correlation function, $w_{\rm p}(r_{\rm p})$ (open circles), and the corresponding real-space correlation function, $\xi(r_{\rm p})$ (red squares), depend on $\pi_{\rm max}$. It is clear that both r_0 and γ are relatively constant in the investigated $\pi_{\rm max}$ range. Our best-fitting values for r_0 and γ are those indicated by the dashed blue line (see Table 1), which corresponds to $\pi_{\rm max} = 10\,h^{-1}$ Mpc.

Our main clustering results, based on the joint X-ray AGN sample, are shown in Fig. 3. The upper panel presents the projected correlation function, while the lower panel presents the redshift-space

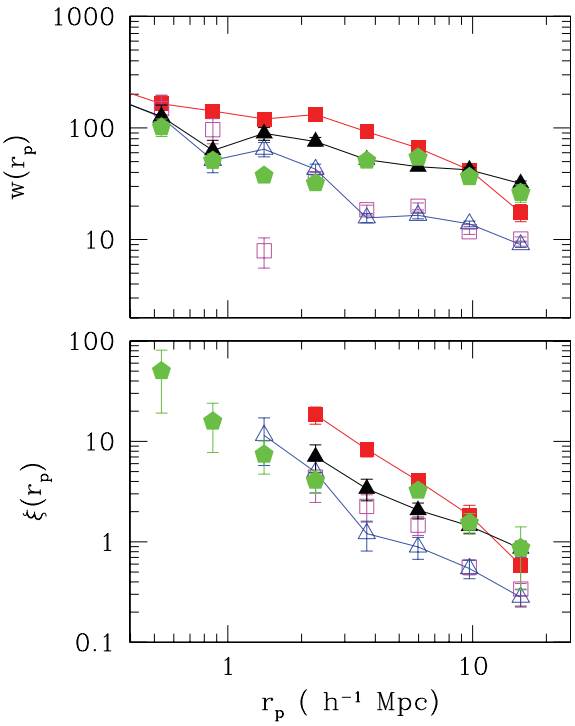

Figure 4. Correlation function of the individual X-ray surveys: CDF-N (green pentagons), CDF-S (red filled squares), ECDF-S (black filled triangles), COSMOS (magenta empty squares), AEGIS (blue empty triangles) for the redshift interval $0 < z < 3$. Upper panel: projected correlation function. Lower panel: the resulting spatial correlation function.

correlation function (circular points) as well as the inferred real-space correlation function, $\xi(r_p)$ (magenta pentagons). The filled circular points are those which have been used to fit the power-law model correlation function, which is shown as a black continuous line (the dashed red line is the power-law fit for a fixed slope of $\gamma = 1.8$). The corresponding best-fitting values for the slope γ and the correlation length are shown in Table 1. The uncertainty of r_0, indicated in Table 1, does not include the effects of cosmic variance, which can be estimated analytically, assuming a power-law correlation function, according to $\sigma^2_{cv} \simeq J_2(\gamma)(r_0/r)^\gamma$, with $J_2(\gamma) = 72/[(3-\gamma)(4-\gamma)(6-\gamma)2^\gamma]$ (Peebles 1980). We find $\sigma_{cv} \simeq 0.3$, which is smaller although of the same order as the fitting uncertainty indicated in Table 1.

We can single out three important results from the clustering analysis of the joint X-ray point-source sample:

(i) the inferred spatial correlation length, from the power-law model fit to equation (6) or directly from equation (7), is ∼20–25 per cent larger than that estimated from the projected correlation function, a fact which is attributed to the correlation function underestimation imposed by the necessary cutoff along the π direction in the projected correlation function measure,

(ii) it appears that redshift-space distortions do not significantly affect the z-space correlation function, since $\xi(s) \simeq \xi(r_p)$, and

(iii) the real-space correlation function, at a median redshift of 0.976, has a slope of $\gamma \simeq 1.5$ and a correlation length of $r_0 \simeq 7.2\,h^{-1}$ Mpc.

4.2 The individual field correlation functions

We now perform the clustering analysis from the previous section in each individual field and compare our results to those from the original studies. To this end we use the redshift interval $0 < z < 3$ and sources with luminosities $L_x \geq 10^{41}$ erg s^{-1} in order to avoid the gross contamination of our X-ray AGN sample by normal galaxies. We estimate the projected and z-space correlation functions in 10 logarithmic intervals of width $\delta \log_{10}(r_p, \pi) = 0.175$ and $\delta \log_{10}(s) = 0.2$, respectively. With the exception of the CDF-N field (see below), the power-law model fit was performed for $r_p \gtrsim 1.5\,h^{-1}$ Mpc in order to avoid the non-linear contributions to the correlation function.

In Fig. 4, we show the projected (upper panel) and the inferred via equation (6) spatial (lower panel) correlation functions of the individual fields, colour coded, while in Table 2 we summarize their best power-law fit parameters γ and r_0. It is evident that the individual determinations of the correlation function are hampered by cosmic variance. It is also interesting to note that the results of the largest survey (COSMOS with ∼1 deg^2 area) are consistent with those of the joint sample (see Table 1).

We find small differences with respect to the results of the original studies, which are mostly due to the slightly different sample definitions and different choices of π_{max}. For example, for the CDF-S field we use the 2 Ms catalogue rather than the 1 Ms catalogue used by G05, while for the CDF-N (Gilli et al. 2005) and for the AEGIS (Coil et al. 2009) samples, the corresponding authors used sources with $L_x \geq 10^{42}$ erg s^{-1}. When using the latter luminosity limit and the original value of π_{max}, we recover the original

Table 2. Parameters of the power-law fits to the different survey correlation functions. The results of the projected correlation function, $w_p(r_p)$, are shown in columns 4 and 5, and of the inferred real-space correlation function, $\xi(r_p)$, in columns 6 and 7. Finally, column 8 shows the correlation length of $\xi(r_p)$ for the average value of the slope $\gamma = 1.44$ (which is practically equal to the slope of the joint sample; see Table 1). In all cases, except for the CDF-N, the power-law fits have been applied to the correlation function data, excluding the non-linear regime ($\lesssim 1.5\,h^{-1}$ Mpc). Since the CDF-N $w_p(r_p)$ shows a knee around $r_p \sim 3.5\,h^{-1}$ Mpc, we present power-law fits for data below and above this scale. Correlation lengths and π_{max} are in h^{-1} Mpc.

Survey	No.	π_{max}	γ	r_0	γ_c	$r_{0,c}$	$r_{0,c}^{\gamma=1.44}$
CDF-N[a]	243	20	1.72 ± 0.30	4.6 ± 0.7	1.66 ± 0.16	5.1 ± 0.6	6.0 ± 0.8
CDF-N[b]	243	20	1.80 ± 0.23	9.9 ± 3.9	1.46 ± 0.22	13.3 ± 4.3	13.3 ± 4.3
CDF-S	219	25	1.90 ± 0.08	10.6 ± 1.4	1.72 ± 0.08	12.8 ± 1.1	15.1 ± 2.1
AEGIS	392	20	1.59 ± 0.09	4.3 ± 0.6	1.22 ± 0.20	5.5 ± 1.0	5.7 ± 0.8
COSMOS	417	25	1.65 ± 0.08	5.5 ± 0.8	1.36 ± 0.15	6.8 ± 1.0	7.0 ± 0.8
ECDF-S	288	10	1.46 ± 0.07	7.6 ± 1.0	1.23 ± 0.16	12.4 ± 2.2	11.1 ± 1.8

[a] $r_p \lesssim 3.5\,h^{-1}$ Mpc.
[b] $r_p > 3.5\,h^{-1}$ Mpc.

clustering results.[1] The only field for which it was not possible to fit a power-law correlation function in the linear scales is the CDF-N field, which presents a knee at $r_p \sim 3.5\,h^{-1}$ Mpc. Therefore, we have performed a power-law fit in the two ranges where such a power-law is exhibited (i.e. for $r_p \lesssim 3.5$ and $>3.5\,h^{-1}$ Mpc, respectively).

The largest clustering amplitude is observed for the CDF-S, a fact which has been attributed to the existence of a large supercluster at $z \simeq 0.7$ (Gilli et al. 2003) and which appears to affect also the corresponding amplitude of the ECDF-S field, the correlation function of which is estimated here for the first time. However, inspecting Fig. 4 and Table 2, it is interesting to note that while the small-scale ($r_p \lesssim 3.5\,h^{-1}$ Mpc) correlation function of CDF-N is consistent with that of both the COSMOS and AEGIS fields, its large-scale correlation function ($r_p > 3.5\,h^{-1}$ Mpc) seems to be consistent with that of the CDF-S and ECDF-S fields. This suggests that either there is some unique structure affecting also the clustering pattern in the CDF-N (although at a lesser extent than in the CDF-S) or there is some unknown systematic affecting both CDFs.

4.3 Luminosity dependence of clustering

We now wish to investigate the possibility of an X-ray luminosity-dependent AGN clustering, as suggested by Plionis et al. (2008). Interestingly, Cappelluti et al. (2010) have found a dependence of clustering on the X-ray luminosity in the sample of local ($\langle z \rangle = 0.05$) X-ray-selected AGN from the *Swift*/BAT survey. Similarly, Krumpe et al. (2010) have also found such indications in the X-ray AGN sample from the *ROSAT* All-Sky Survey.

The five X-ray surveys that we have analysed in the previous sections, although they cover a similar redshift range, have X-ray luminosity distributions which are quite different. To disentangle the luminosity and redshift dependence of clustering, we construct a low-L_x and a high-L_x (X-ray luminosity) subsample for each survey. We also impose them to have the same redshift distribution. This is achieved by first splitting the sources according to the selected luminosity limit and then matching their binned redshift distribution in the common area. We do so by randomly selecting sources from the most abundant L_x subsample so as to reproduce exactly the shape of the binned redshift distribution of the less abundant subsample. The bin size used is $\delta z = 0.05$. This random selection process is performed eight times and the final results are the average over these eight realizations.

As an example of our procedure we show in Fig. 5 the redshift distribution of the whole AEGIS field (black thick line), dividing it also into its two luminosity subsamples, i.e. the low-L_x subsample with $L_x < 10^{43}$ erg s^{-1} (black dense-shaded histogram) and a high-L_x subsample with $L_x \geq 10^{43}$ erg s^{-1} (red sparse-shaded histogram). In the inset panel we also show the X-ray luminosity distribution of the AEGIS field, where a clear division can be observed at $L_x \simeq 10^{43}$ erg s^{-1}. Finally, the left-hand panel of Fig. 6 shows the redshift distribution of the low-L_x and high-L_x subsamples in the common redshift range ($0.5 < z < 1.5$), while in the right-hand panel we present one random realization of the matched z-distributions of the two subsamples, which are those finally used to estimate the correlation function of the low-L_x and high-L_x subsamples. It is evident that our procedure has managed to create subsamples

[1] Due to the fact that in the luminosity-dependent analysis of the next section we are left with a small number of sources, we are obliged to lower the X-ray luminosity limit to $L_x = 10^{41}$ erg s^{-1}.

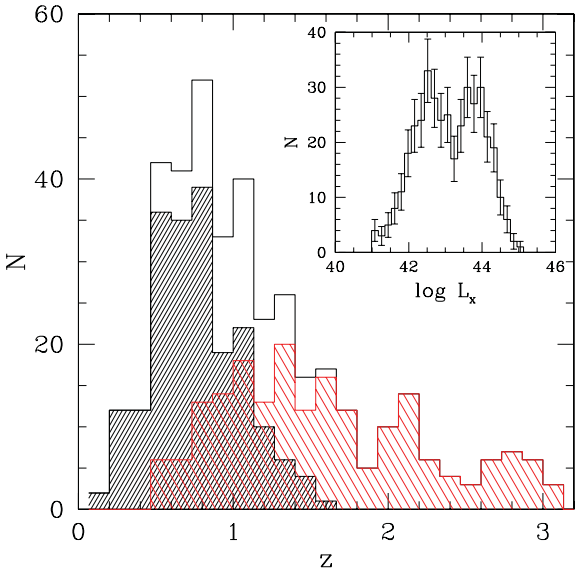

Figure 5. The redshift distribution of the AEGIS sources (thick black line histogram) also divided into the two luminosity subsamples (low-L_x: black dense-shaded histogram; high-L_x: red sparse-shaded histogram). The inset panel shows the X-ray luminosity distribution. The trough between the two apparent peaks, at $L_x \simeq 10^{43}$ erg s^{-1}, defines the division value between the low-L_x and high-L_x subsamples.

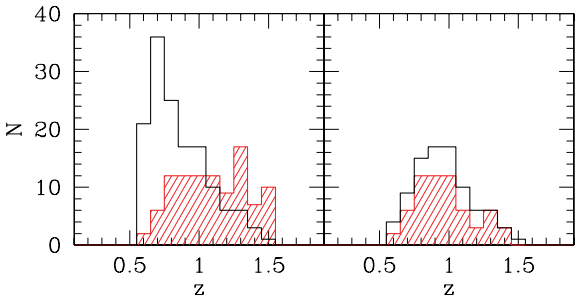

Figure 6. Left-hand panel: redshift distribution at the common interval $z = 0.5$–1.5 of the low-L_x (black line) and high-L_x (red shade) subsamples. Right-hand panel: the matched redshift distributions of the further reduced subsamples, according to the method described in the text imposed in order to cancel redshift-dependent effects in their correlation function comparison.

that have a common redshift distribution, therefore suppressing any redshift-dependent effect in the comparison of the clustering results of the low-L_x and high-L_x AGN subsamples.

We then use the χ^2 minimization procedure to fit a power-law model to the measured $w_p(r_p)$ of the low-L_x and high-L_x subsamples, typically in the projected separation range $r_p \in [0.16$–$10]\,h^{-1}$ Mpc. Note that it is not possible to exclude in this analysis the non-linear scales ($\lesssim 1.5\,h^{-1}$ Mpc) due to the small number of sources involved and the consequent noisy correlation function. Furthermore, and in order to be able to compare the different results on an equal footing, we present the inferred spatial correlation length, based on a power-law fit to the $\xi(r_p)$ (equation 6) for a common slope, which is the mean of the low-L_x and high-L_x subsample $\xi(r_p)$ slopes.

The results of the correlation function analysis for the low-L_x and high-L_x subsamples of the individual X-ray surveys can be found in Table 3. In Fig. 7 we present the inferred spatial clustering length, $r_{0,c}$, as a function of the X-ray luminosity. There are indications of a luminosity-dependent clustering in all X-ray surveys, except for the CDF-S in which the correlation lengths for both low-L_x and

Table 3. Correlation function results from the X-ray luminosity separated subsamples for each individual X-ray survey. Note that due to the small samples involved we have used different bin sizes for each sample in order to minimize the intrinsic scatter. Note also that the following redshift intervals were used – CDF-N: $0.5 < z < 1.2$; CDF-S: $0.7 < z < 1.4$; AEGIS: $0.5 < z < 1.5$; COSMOS: $0.6 < z < 1.8$; ECDF-S: $0.7 < z < 1.6$. The last two columns list the slope (averaged over the two luminosity subsamples) and amplitude of the power-law fit to the spatial correlation function, $\xi(r_{\rm p})$, of equation (6).

$\log_{10}L_x$	No.	$\bar{z}$	$\pi_{\rm max}$	γ	r_0	$\gamma_{\rm c}$	$r_{0,\rm c}$
			CDF-N				
$\leq$42.2	73	0.84	10	1.74 ± 0.15	3.4 ± 0.4	1.36	4.7 ± 0.7
>42.2	79	0.96	10	1.42 ± 0.16	4.5 ± 1.1	1.36	7.2 ± 1.1
			CDF-S				
$\leq$42.5	53	0.95	10	1.97 ± 0.20	10.0 ± 2.5	1.54	16.5 ± 2.3
>42.5	44	1.02	10	1.65 ± 0.15	9.3 ± 2.3	1.54	13.6 ± 2.6
			AEGIS				
$\leq$43	90	0.83	20	2.03 ± 0.29	4.6 ± 1.5	1.83	5.1 ± 1.3
>43	63	0.82	20	1.90 ± 0.30	5.7 ± 2.1	1.83	6.4 ± 1.8
			COSMOS				
$\leq$43.5	72	1.06	30	2.00 ± 0.13	6.6 ± 1.3	1.85	7.6 ± 1.5
>43.5	51	1.07	30	2.00 ± 0.23	10.3 ± 3.0	1.85	11.9 ± 3.0
			ECDF-S				
$\leq$43.2	51	1.04	30	1.91 ± 0.36	5.9 ± 2.5	1.85	6.3 ± 2.5
>43.2	30	1.02	30	1.98 ± 0.28	7.7 ± 3.0	1.85	8.6 ± 3.0

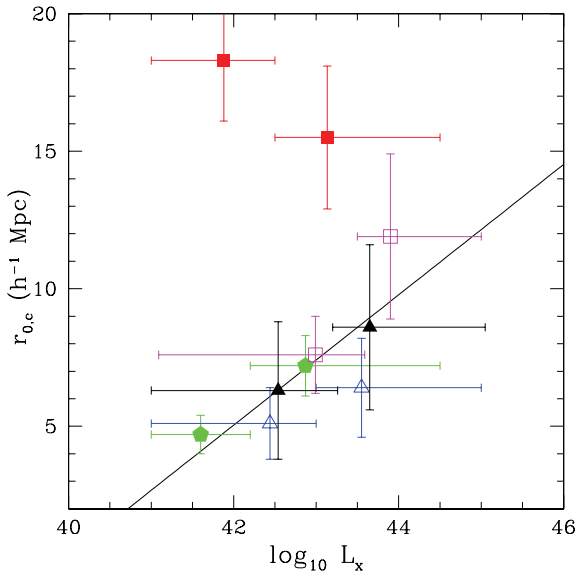

Figure 7. Spatial clustering length, $r_{0,\rm c}$, estimated from equation (6), as a function of the X-ray luminosity for the different surveys. The colour code and symbols are the same as in Fig. 4. The black line is the best linear fit to the data, excluding the CDF-S (red circles) results.

high-L_x subsamples are atypically very high (probably due to the dominance of a known supercluster; Gilli et al. 2003). Although the luminosity-dependent clustering indications in each of the four remaining X-ray fields are rather weak, there is an overall suggestive and systematic trend with the high-L_x subsamples being more strongly clustered than the lower L_x ones. A linear least-squares fit to the data of Fig. 7, taking into account the uncertainties in both axes and excluding the CDF-S, provides the dependence $r_{0,\rm c}/(h^{-1}\,{\rm Mpc}) \simeq 2.4 \log_{10} L_x - 94.7$. This is indicated by the thick continuous line in Fig. 7. The relatively strong trend implied by this relation, although the individual survey luminosity-dependence results are not that significant, is due to the fact that in each field a different high- and low-luminosity range is sampled, increasing the X-ray luminosity dynamical range.

5 BIAS AND HOST HALO MASS

It is well established that the extragalactic sources are biased tracers of the underlying mass fluctuation field (e.g. Bardeen et al. 1986; Kaiser 1987). The parameter that encapsulates this fact is the so-called linear bias factor, b, defined as the ratio of the fluctuations of some mass tracer, here the AGN ($\delta_{\rm AGN}$), to those of the underlying DM mass ($\delta_{\rm DM}$),

$$b = \frac{\delta_{\rm AGN}}{\delta_{\rm DM}} \,. \tag{10}$$

Since the correlation function is generally defined as $\xi(r) = \langle \delta(\boldsymbol{x})\delta(\boldsymbol{x}+\boldsymbol{r})\rangle$ (the so-called *Poisson process* definition), an equivalent definition of the bias parameter is the square root of the ratio of the two-point correlation function of AGN to that of the underlying mass,

$$b = \left(\frac{\xi_{\rm AGN}}{\xi_{\rm DM}}\right)^{1/2} . \tag{11}$$

Another related definition, which is the one that will be used in the current work, is the ratio of the variances of the AGN and underlying mass density fields, smoothed at some linear scale,

$$b = \frac{\sigma_{8,\rm AGN}}{\sigma_{8,\rm DM}}, \tag{12}$$

where $\sigma_{8,\rm AGN}$ is the rms fluctuations of the AGN density distribution within spheres of a comoving radius of $8\,h^{-1}$ Mpc, given under the assumption of power-law correlations by Peebles (1980),

$$\sigma_{8,\rm AGN} = J_2(\gamma)^{\frac{1}{2}} \left(\frac{r_0}{8}\right)^{\frac{\gamma}{2}} , \tag{13}$$

and $\sigma_{8,\rm DM}$ is the variance of the DM density fluctuation field which evolves according to (e.g. Peebles 1993)

$$\sigma_{8,\rm DM}(z) = \sigma_8 \frac{D(z)}{D(0)} , \tag{14}$$

with $D(z)$ the linear growth factor, which for the concordance Λ cosmology is given by (Peebles 1993)

$$D(z) = \frac{5\Omega_{\rm m} E(z)}{2} \int_z^\infty \frac{(1+y)}{E^3(y)} {\rm d}y \,. \tag{15}$$

Combining equations (12)–(14), we obtain the cosmological evolution of biasing as a function of the power-law clustering parameters,

$$b(z) = \left(\frac{r_0}{8}\right)^{\frac{\gamma}{2}} J_2^{\frac{1}{2}} \left(\frac{\sigma_8 D(z)}{D(0)}\right)^{-1}. \quad (16)$$

Finally, an alternative approach to estimate the bias, free of the power-law clustering assumption, is provided by the square root of the ratio of the projected AGN correlation function to the two-halo term of the theoretical projected correlation function, based on the Fourier transform of the linear cold dark matter (CDM) power spectrum (e.g. Allevato et al. 2011; Miyaji et al., 2011; Krumpe et al. 2012). These authors have used both of the latter two approaches to estimate the bias and have shown that they provide mutually consistent results, with a possible systematic uncertainty of ∼20 per cent, which is however within their respective uncertainties.

The CDM structure formation scenario predicts that the bias factor is determined by the mass of the DM halo within which the extragalactic mass tracer forms (e.g. Mo & White 1996). In order to assign a characteristic DM halo mass to the estimated bias factors, we use two bias evolution models, the Tinker et al. (2010) model (hereafter TRK) and the Basilakos, Plionis & Ragone-Figueroa (2008) model (hereafter BPR). The former, an improvement of the original Sheth & Tormen (1999) model, belongs to the so-called *galaxy merging* bias family, which is based on the Press & Schechter (1974) formalism, the peak-background split (Bardeen et al. 1986) and the spherical collapse model (e.g. Sheth & Tormen 1999; Valageas 2009, 2011). The latter is an extension of the so-called *galaxy conserving* bias models, and uses linear perturbation theory and the Friedmann–Lemaitre solutions to derive a second-order differential equation for the evolution of bias, assuming that the tracer and the underlying mass share the same dynamics. Furthermore, the model includes the contribution of an evolving DM halo population, due to processes like merging. Details of these models, as well as a comparison among five current bias evolution models, can be found in Papageorgiou et al. (2012).

5.1 X-ray AGN bias

When applying the above analysis to the clustering results of our joint X-ray sample (with a median redshift of $\langle z \rangle \simeq 0.98$), we find a bias factor of $b \simeq 2.26 \pm 0.16$. This value corresponds to a DM halo mass of $\log_{10}(M_{\rm h}/[h^{-1}\,{\rm M}_\odot]) \simeq 13.06(\pm 0.13)$ and $13.19(\pm 0.08)$ for the BPR and TRK models, respectively (the first row of Table 4). We also extend the same analysis to the low-L_x and high-L_x AGN subsamples in each X-ray field separately. As expected by the dependence of the correlation function on luminosity that we presented in Section 4.3, the high-L_x subsamples provide larger bias factors and correspondingly larger DM halo masses (for both the BPR and TRK bias models) than the low-L_x subsamples. An exception is the CDF-S field, which as we have already discussed is hampered by the presence of a large supercluster (Gilli et al. 2003). Thus, the data seem to suggest that high-L_x sources inhabit more massive DM haloes than low-L_x sources. The results listed in Table 4 indicate that for an average luminosity difference of $\langle \delta \log_{10} L_x \rangle \simeq 1$ between the high-L_x and low-L_x AGN subsamples, the corresponding average DM halo mass of the former sample is a factor of ∼3 larger than that of the latter.

Similar results have been found by Cappelluti et al. (2010) for a sample of X-ray-selected AGN from the *Swift*/BAT survey. These authors derive for AGN with $L_x < 10^{44}\,{\rm erg\,s^{-1}}$ a DM host halo mass of $\log_{10}(M_{\rm h}/[h^{-1}\,{\rm M}_\odot]) \approx 10^{12}\,{\rm M}_\odot$, while for AGN with $L_x \geq 10^{44}\,{\rm erg\,s^{-1}}$ they find a DM host halo mass of $\sim 10^{14}\,h^{-1}\,{\rm M}_\odot$.

Table 4. The bias corresponding to the clustering of the joint sample (1466 sources) and of the luminosity divided subsamples for each individual X-ray survey studied. The corresponding values of the halo mass, in units of $\log_{10}(M_{\rm h}/[h^{-1}\,{\rm M}_\odot])$ are estimated using a *Wilkinson Microwave Anisotropy Probe* 7 (*WMAP*7) cosmology, i.e. $\sigma_8 = 0.81$ and $\Omega_{\rm m} = 0.273$, and are based on the BPR (fourth column) and TRK (fifth column) bias evolution models.

$\log_{10}L_x$	$\overline{\log_{10} L_x}$	$\bar{z}$	$b(\bar{z})$	BPR	TRK
		Joint			
		0.98	2.26 ± 0.16	$13.06^{+0.12}_{-0.14}$	$13.19^{+0.07}_{-0.09}$
		CDF-N			
≤42.2	41.84	0.84	1.52 ± 0.17	$12.38^{+0.29}_{-0.40}$	$12.26^{+0.23}_{-0.30}$
>42.2	43.18	0.96	2.15 ± 0.24	$12.99^{+0.20}_{-0.24}$	$12.79^{+0.19}_{-0.21}$
		CDF-S			
≤42.5	42.19	0.95	4.22 ± 0.47	$14.07^{+0.15}_{-0.17}$	$13.86^{+0.11}_{-0.12}$
>42.5	43.45	1.02	3.75 ± 0.56	$13.80^{+0.20}_{-0.25}$	$13.52^{+0.17}_{-0.21}$
		AEGIS			
≤43	42.75	0.89	1.74 ± 0.41	$12.65^{+0.45}_{-0.84}$	$12.49^{+0.39}_{-0.64}$
>43	43.86	0.89	2.14 ± 0.55	$13.09^{+0.41}_{-0.68}$	$12.87^{+0.35}_{-0.57}$
		COSMOS			
≤43.5	43.30	1.07	2.72 ± 0.50	$13.24^{+0.27}_{-0.36}$	$13.04^{+0.24}_{-0.33}$
>43.5	44.21	1.07	4.12 ± 0.96	$13.86^{+0.29}_{-0.39}$	$13.59^{+0.24}_{-0.34}$
		ECDF-S			
≤43.2	42.86	1.03	2.25 ± 0.83	$12.96^{+0.54}_{-1.16}$	$12.79^{+0.47}_{-0.97}$
>43.2	43.97	1.03	3.00 ± 0.97	$13.46^{+0.42}_{-0.70}$	$13.22^{+0.37}_{-0.62}$

Table 5. The values of the X-ray AGN bias factor in redshift bins. Above $z = 2$ the correlation function was extremely noisy and impossible to determine. The halo masses shown are estimated using a *WMAP*7 cosmology, i.e. $\sigma_8 = 0.81$ and $\Omega_{\rm m} = 0.273$ and for three different models of bias evolution (see also Papageorgiou et al. 2012).

No.	z-range	$\bar{z}$	$b(\bar{z})$	$\log_{10}(M_{\rm h}/[h^{-1}\,{\rm M}_\odot])$ BPR	TRK
353	0.00–0.67	0.488	1.71 ± 0.23	$13.37^{+0.27}_{-0.36}$	$13.00^{+0.21}_{-0.29}$
354	0.67–0.96	0.787	2.46 ± 0.25	$13.52^{+0.16}_{-0.19}$	$13.22^{+0.14}_{-0.16}$
352	0.96–1.38	1.123	2.46 ± 0.23	$13.00^{+0.16}_{-0.18}$	$12.90^{+0.10}_{-0.22}$
200	1.38–2.00	1.613	3.85 ± 1.55	$13.09^{+0.48}_{-0.88}$	$13.00^{+0.43}_{-0.82}$

Krumpe et al. (2010) also find evidence for luminosity dependence in a sample of the *ROSAT* All-Sky Survey AGN. In particular, they find $\log_{10}(M_{\rm h}/[h^{-1}\,{\rm M}_\odot]) = 11.83$ and 13.10 for their low and high X-ray luminosity AGN sources (below and above $L_{0.1-2.4{\rm keV}} = 10^{44.3}\,{\rm erg\,s^{-1}}$), respectively.

5.2 Bias evolution

In order to investigate the redshift evolution of the bias factor, we split the whole sample into four redshift bins. The resulting values of the bias factor in each bin, as well as the typical DM halo masses, based on the two previously mentioned models, are shown in Table 5. Fig. 8 (left-hand panel) shows our determination of the bias in the different redshift bins together with the corresponding results of the *XMM*–COSMOS (Allevato et al. 2011), the Xbootes (Starikova et al. 2011), the *ROSAT* (Krumpe et al. 2010) and the *Swift*/BAT (Cappelluti et al. 2010) surveys. The increase of the bias

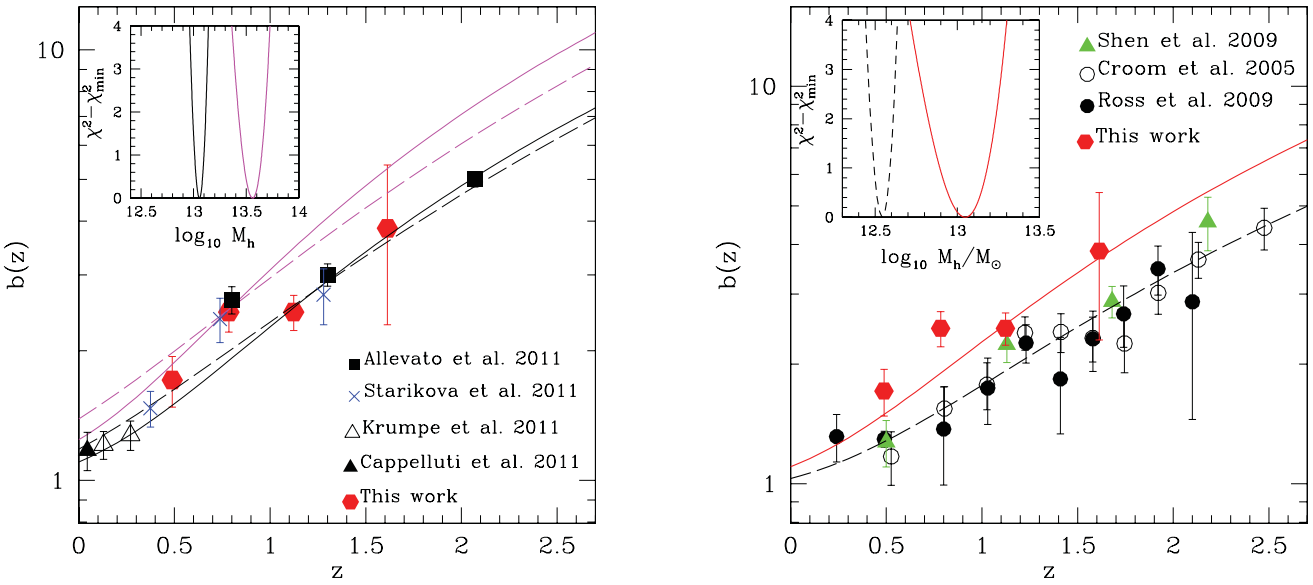

Figure 8. Left-hand panel: comparison of the redshift evolution of the bias parameter of our joint X-ray sample (red pentagons) with that of other X-ray surveys. The point and colour coding of the results based on different surveys is indicated by the corresponding labels. The theoretical bias evolution models, fitted to the data for a single DM halo mass, are shown as continuous or dashed lines. The black continuous line is the best-fitting BPR bias evolution model to all the bias data, excluding the deviant points at $z \sim 0.75$, while the dashed line is the corresponding best-fitting TRK model. The magenta continuous and dashed lines are the fits of the corresponding two models to the bias values around $z \sim 0.75$. In the inset panel we show the best-fitting DM halo mass value as a function of $\chi^2 - \chi^2_{\rm min}$ for the BPR model. A value of $\chi^2 - \chi^2_{\rm min} = 1$ or 4 corresponds to the 1σ or 2σ uncertainty in the fitted parameter (for the case of one free parameter). Right-hand panel: comparison of the redshift evolution of the bias parameter of the joint X-ray sample (red pentagons) to that of optical QSOs. The point and colour coding of the results based on different surveys is indicated by the corresponding labels. The curves correspond to the BPR bias evolution model fitted to the X-ray data (red continuous line) and to the optical QSO (black dashed line). Note that the plotted bias values are rescaled to the *WMAP*7 cosmology, as in Papageorgiou et al. (2012).

factor with increasing redshift is evident, as well as the consistency of the derived bias values of the different studies at the corresponding redshifts.

Allevato et al. (2011) have argued that models of bias evolution based on a single host halo mass cannot explain their results, but rather there are indications for different halo masses hosting X-ray AGN at the different redshifts. We check their suggestion by applying the previously mentioned bias evolution models and attempting to fit a single halo mass jointly to all the previously mentioned bias data. Indeed, no such model can fit adequately well the results (the resulting reduced χ^2 is $\gtrsim 1.6$). The cause of this failure is mostly the deviant bias values around $z \sim 0.75$. If this redshift bin is excluded, then the bias data can indeed be fitted by a single host halo mass with $\log_{10}(M_{\rm h}/[h^{-1}\,{\rm M}_\odot]) \simeq 13.06 \pm 0.04$, χ^2/d.o.f.=0.24 and a present epoch bias of $b(0) = 1.1$ (black continuous line in Fig. 8) for the BPR model. For the TRK model we find $\log_{10}(M_{\rm h}/[h^{-1}\,{\rm M}_\odot]) \simeq 12.94 \pm 0.05$, χ^2/d.o.f.=0.48 and $b(0) = 1.18$ (black dashed line in Fig. 8). If we use, however, only the three deviant bias values around $z \simeq 0.75$, we find $\log_{10}(M_{\rm h}/[h^{-1}\,{\rm M}_\odot]) \simeq 13.56 \pm 0.09$, χ^2/d.o.f.=0.29 and $b(0) = 1.24$ (magenta continuous line) for the BPR model, and $\log_{10}(M_{\rm h}/[h^{-1}\,{\rm M}_\odot]) \simeq 13.28 \pm 0.10$, χ^2/d.o.f.=0.29 and $b(0) = 1.39$ (magenta dashed line) for the TRK model. It is interesting to point out that the bias values of the current study (red pentagons), when excluding the deviant point, provide exactly the same fit as the one obtained previously, using all the determinations of the bias evolution values (again excluding the deviant points). However, the uncertainty is, as expected, larger [for example, for the BPR model we obtain $\log_{10}(M_{\rm h}/[h^{-1}\,{\rm M}_\odot]) \simeq 13.08 \pm 0.14$ with χ^2/d.o.f.=0.48].

5.3 X-ray versus optically selected AGN

We also compare in the right-hand panel of Fig. 8 our X-ray AGN results with the bias of optically selected QSO, based on the 2dF spectroscopic sample of 20 000 QSOs (Croom et al. 2005), on an SDSS (Data Release 5 [DR5]) QSO sample of ∼30 000 spectroscopic QSO with $z \lesssim 2.2$ (Ross et al. 2009) and on a homogeneous sample of ∼38 000 SDSS QSOs with $0.1 \leq z \leq 5$ (Shen et al. 2009). Since the X-ray data do not extend to such high redshifts and in order to consistently compare optical and X-ray bias data, we choose to exclude the very high z ($3 < z < 4.5$) optical bias data of Shen et al. Note also that since each of the optical QSO studies has used a slightly different flat ΛCDM background cosmology, the bias values shown in Fig. 8 have been scaled to the *WMAP*7 cosmology, following the prescription of Papageorgiou et al. (2012). The results of each of the different studies are indicated in the figure with distinct colours and symbol types.

The BPR model that fits simultaneously all the optical QSO bias data provides a DM halo mass of $\log_{10}(M_{\rm h}/[h^{-1}\,{\rm M}_\odot]) \simeq 12.50 \pm 0.05$ with χ^2/d.o.f.=0.68. The corresponding values for the TRK bias model are practically the same: $\log_{10}(M_{\rm h}/[h^{-1}\,{\rm M}_\odot]) \simeq 12.49 \pm 0.04$ with χ^2/d.o.f.=0.64. It is therefore evident that the X-ray-selected AGN bias values, and the corresponding DM halo masses, are significantly larger than those of the optical QSO, indicating that they probably constitute separate families of AGN, each probably having a distinct BH fuelling mechanism. Allevato et al. (2011) also conclude that the DM haloes in which X-ray-selected AGN reside are more massive than those of optically selected QSOs. Further below we will provide a tentative explanation for such a difference between the host haloes of optical and X-ray-selected AGN.

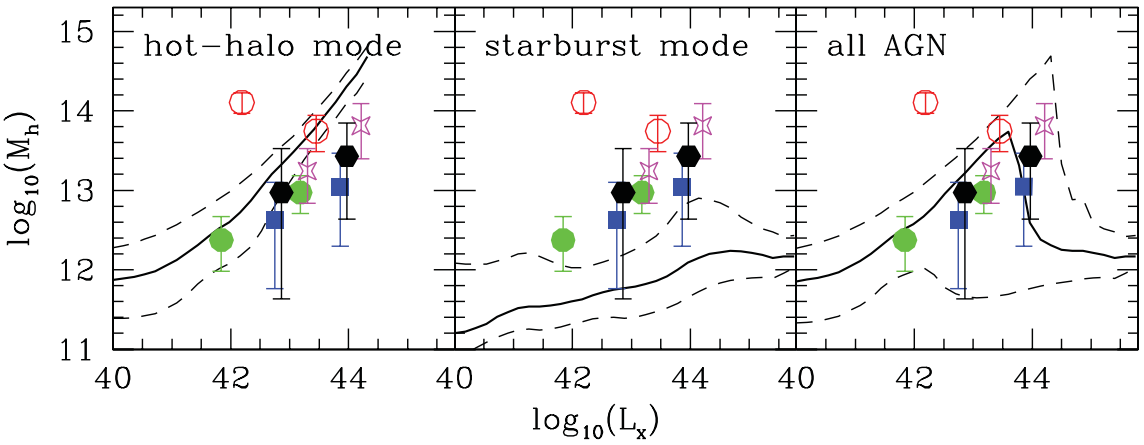

Figure 9. The median X-ray luminosity (0.5–8 keV) of the luminosity separated subsamples (from Table 4) versus the DM halo mass predicted by the TRK bias model. The colour coding is the same as in Fig. 4. For comparison we show the theoretical predictions of the Fanidakis et al. (2012) BH model at $z = 0.5$–1.5. The solid lines indicate the median of the $\log L_{\rm x} - \log M_{\rm h}$ correlation for AGN accreting from the hot halo (hot-halo mode; left-hand panel), or during disc instabilities and mergers (starburst mode; middle panel) and all AGN in their model (right-hand panel). The dashed lines indicate the 10−90 percentiles around the median.

6 COMPARISON WITH AGN ACCRETION MODELS

Our analysis provides new insights into the host DM haloes of moderate-luminosity X-ray-selected AGN. By fitting two different bias evolution models, we find that the AGN in our samples inhabit DM haloes with masses of $\log_{10}(M_{\rm h}/[h^{-1}\,{\rm M}_{\odot}]) \simeq 13.1 \pm 0.1$. The estimated halo mass is significantly higher than the typical halo mass of optically selected QSO [$\log_{10}(M_{\rm h}/[h^{-1}\,{\rm M}_{\odot}]) \sim 12.5$; see Fig. 8]. Similar results are also found in other X-ray studies (e.g. Coil et al. 2009; Allevato et al. 2011; Starikova et al. 2011; Mountrichas & Georgakakis 2012), and therefore the DM halo masses estimated in most X-ray surveys are consistent mostly with those of elliptical/red galaxies. This implies that the fuelling mechanism of the moderate-luminosity X-ray-selected AGN and that of the more luminous optically selected QSOs are different.

Semi-analytic models that assume major mergers as the main mechanism for triggering AGN activity predict that the mass of DM haloes that host AGN is lower than that estimated from observations of moderate-luminosity X-ray AGN (e.g. Bonoli et al. 2009; Marulli et al. 2009). The theoretical predictions from these models are more consistent with the halo mass of optically selected QSOs. Additional evidence against the major-merger scenario in moderate-luminosity X-ray AGN comes from the morphological analysis of AGN in the AEGIS and COSMOS surveys (Georgakakis et al. 2009; Silverman et al. 2009). These authors find that X-ray-selected AGN span a large range of environments and morphologies with roughly equal numbers of bulges, spirals and morphologically disturbed galaxies (see also Cisternas et al. 2011; Schawinski et al. 2011; Kocevski et al. 2012). Also, stochastic accretion models (Hopkins & Hernquist 2006) cannot explain large DM haloes for moderate-luminosity AGN. According to these models, disc instabilities and minor interactions feed at high accretion rates relatively small BHs. These models predict that moderate-luminosity AGN reside in low-density environments, similar to those of blue star-forming galaxies.

Regarding the luminosity dependence of the clustering of X-ray-selected AGN (and consequent luminosity dependence of the host halo mass), various theoretical models of BH and galaxy co-evolution predict only a weak dependence of AGN clustering on luminosity (e.g. Hopkins et al. 2005; Hopkins & Hernquist 2006; Lidz et al. 2006). In these models, both the bright and faint AGN reside in similar mass haloes. The bright AGN correspond to BHs that radiate at their peak luminosities, i.e. at accretion rates close to the Eddington ones. In contrast, the faint end of the AGN luminosity function consists of AGN in dimmer (late) phases in their evolution.

Our derived DM halo masses of X-ray-selected AGN could suggest, as Mountrichas & Georgakakis (2012) also point out, a fuelling mechanism similar to that of Ciotti & Ostriker (2001). The authors suggest that stellar winds in early-type galaxies provide the gas supply to the BH (see also Kauffmann & Heckman 2009). Alternatively, another plausible model is that of Bower et al. (2006), where gas is accreted on to BHs directly from the hot halo of the galaxy. Fanidakis et al. (2012) recently presented a calculation for accreting BHs within the Bower et al. (2006) semi-analytic model, where AGN activity is coupled to the evolution of the host galaxy. The authors assume that BHs grow via accretion triggered by galaxy mergers and disc instabilities (starburst mode), as well as accretion of hot gas from the halo of the galaxy (hot-halo mode). In Fig. 9, we compare our halo mass estimates for the individual subsamples in Table 5 with the predictions of the Fanidakis et al. (2012) model for the $L_x - M_{\rm h}$ correlation at $z = 0.5$–1.5. Their calculations assume a flat cosmology with $\Omega_{\rm m} = 0.25$, $\Omega_{\rm b} = 0.045$, $\sigma_8 = 0.9$ and $h = 0.7$, and for consistency, we re-estimated the DM halo mass values according to their adopted cosmology.

As illustrated in the left-hand panel of Fig. 9, the Fanidakis et al. model predicts a strong X-ray luminosity–halo mass correlation for AGN accreting in the hot-halo mode. In contrast, the halo mass of AGN in the starburst mode shows a very modest increase to X-ray luminosities of $L_{\rm x} \simeq 10^{44}{\rm ergs}^{-1}$, beyond which it remains constant and approximately equal to $10^{12}\,{\rm M}_{\odot}$ (middle panel). When considering all the AGN in the model, the shape of the correlation is dominated by the hot-halo mode in the low luminosity and by the starburst mode in the high-luminosity regime (right-hand panel). Thus, the resulting correlation increases steeply in the moderate-luminosity regime and then sharply declines and flattens for the brightest luminosities. Our X-ray-selected AGN results appear to be in very good agreement with the predictions of the Fanidakis et al. model. The data lie in the region of the $L_{\rm x} - M_{\rm h}$ plane, which is dominated by the hot-halo mode. This suggests that intermediate-luminosity AGN are preferentially powered by accretion of gas from the hot halo. Their model further proposes that sources with $L_{\rm x} \gtrsim 10^{44}$ ergs^{-1}, expected to be visible as QSOs, live in haloes with

masses of $\sim 10^{12}$ $M_{\odot}$ as suggested by clustering studies of optically selected QSOs (see Fig. 8, right-hand panel).

The distinctive environmental dependence of the starburst and hot-halo modes in the Fanidakis et al. model is linked to the cooling properties of the gas in DM haloes (White & Frenk 1991). In the starburst mode, disc instabilities and galaxy mergers take place in gas-rich environments. In the standard ΛCDM paradigm, this corresponds to intermediate-mass DM haloes, where gas cools rapidly. In more massive haloes, the gas is in quasi-hydrostatic equilibrium and therefore characterized by a significant lower cooling efficiency. In addition, in this mass regime AGN feedback reheats the gas in the halo, shutting off the cooling completely. AGN activity maximizes at the transition between the rapid-cooling and quasi-hydrostatic regimes, which in the Fanidakis et al. model is found to take place at $M_{\rm h} \sim 10^{12}$ $M_{\odot}$. In haloes more massive than $\sim 10^{12}$ $M_{\odot}$, BHs accrete low-density gas directly from the hot halo. In this case, the authors assume that the amount of gas that is accreted on to the BH is determined by, and in fact is proportional to, the cooling luminosity of the gas in the halo (see Bower et al. 2006; Fanidakis et al. 2011). Since the cooling luminosity increases with increasing halo mass, their model predicts a strong correlation between accretion luminosity and DM halo mass. The good agreement of the predictions of these accretion prescriptions with our analysis, and also with the clustering results of optically selected QSOs, strengthens the idea of two distinct fuelling modes: the hot-halo mode in moderate-X-ray AGN and the starburst mode in the more luminous optical QSOs.

7 SUMMARY

We use 1466 X-ray-selected AGN in the 0.5–8 keV band with spectroscopic redshifts spanning the redshift interval $0 < z < 3$, with a median of $\bar{z} = 0.976$. We derive a spatial clustering length of $r_0 = 7.2 \pm 0.6\,h^{-1}$ Mpc and a slope of $\gamma = 1.47 \pm 0.12$. The corresponding clustering length for the nominal slope of $\gamma = 1.8$ is $r_0 = 6.5 \pm 0.4\,h^{-1}$ Mpc. The above clustering length corresponds to a bias of $b(\bar{z}) = 2.26 \pm 0.16$, translating into a mass of the host DM halo of $M_{\rm h} \sim 1.3 \times 10^{13}\,h^{-1}\,M_{\odot}$. The derived bias and the corresponding host halo mass of X-ray-selected AGN are significantly higher than those of optically selected AGN. This may imply a different fuelling mechanism for X-ray-selected AGN in comparison to optically selected AGN. We also find indications for a dependence of the clustering strength on the X-ray luminosity, when we consider AGN at a redshift of $z \sim 1$. The more X-ray luminous the sources are, the larger, typically, the clustering length and hence the higher the DM host halo mass is. For an average luminosity difference of $\langle \delta \log_{10} L_x \rangle \simeq 1$, between the high-$L_x$ and low-L_x AGN subsamples, the corresponding average DM halo mass of the former sample is a factor of $\sim$3 larger than that of the latter.

The luminosity-dependent clustering that we find seems to be in favour of a BH accretion model where moderate-luminosity X-ray AGN, at $z \sim 1$, are fuelled mostly by accretion from the hot halo around the host galaxy. The good agreement of the model predictions with similar studies in the optical further suggests that luminous quasar activity is triggered in lower mass halo (and gas-rich) environments by disc instabilities and galaxy mergers.

ACKNOWLEDGMENTS

We thank Alison Coil for providing us with the spectroscopic data of the AEGIS field, as well as for useful comments on the paper. Part of this work was supported by the COST Action MP0905 'Black Holes in a Violent Universe'.

REFERENCES

Akylas A., Georgantopoulos I., Plionis M., 2000, MNRAS, 318, 1036
Alexander D. M. et al., 2003, AJ, 126, 539
Allevato V. et al., 2011, ApJ, 736, 99
Bardeen J. M., Bond J. R., Kaiser N., Szalay A. S., 1986, ApJ, 304, 15
Basilakos S., Georgakakis A., Plionis M., Georgantopoulos I., 2004, ApJ, 607, L79
Basilakos S., Plionis M., Georgakakis A., Georgantopoulos I., 2005, MNRAS, 356, 183
Basilakos S., Plionis M., Ragone-Figueroa C., 2008, ApJ, 678, 627
Bonoli S., Marulli F., Springel V., White S. D. M., Branchini E., Moscardini L., 2009, MNRAS, 396, 423
Bournaud F., Dekel A., Teyssier R., Cacciato M., Daddi E., Juneau S., Shankar F., 2011, ApJ, 741, L33
Bower R. G., Benson A. J., Malbon R., Helly J. C., Frenk C. S., Baugh C. M., Cole S., Lacey C. G., 2006, MNRAS, 370, 645
Bradshaw E. J. et al., 2011, MNRAS, 415, 2626
Brusa M. et al., 2010, ApJ, 716, 348
Cappelluti N., Ajello M., Burlon D., Krumpe M., Miyaji T., Bonoli S., Greiner J., 2010, ApJ, 716, L209
Carrera F. J. et al., 2007, A&A, 469, 27
Ciotti L., Ostriker J. P., 2001, ApJ, 551, 131
Cisternas M. et al., 2011, ApJ, 726, 57
Coil A. L. et al., 2009, ApJ, 701, 1484
Croom S. M. et al., 2005, MNRAS, 356, 415
Croton D. J. et al., 2006, MNRAS, 365, 11
da Ângela J. et al., 2008, MNRAS, 383, 565
Davis M., Peebles P. J. E., 1983, ApJ, 267, 465
Davis M., Newman J. A., Faber S. M., Phillips A. C., 2001, in Cristiani S., Renzini A., Williams R. E., eds, Deep Fields: The DEEP2 Redshift Survey. Springer-Verlag, p. 241
Davis M. et al., 2003, inGuhathakurta P., ed., Proc. SPIE, 4834, 161
Di Matteo T., Springel V., Hernquist L., 2005, in Merloni A., Nayakshin S., Sunyaev R. A., eds, Growing Black Holes: Accretion in a Cosmological Context, Black Holes in Galaxy Mergers. Springer-Verlag, Berlin/Heidelberg, p. 340
Ebrero J., Mateos S., Stewart G. C., Carrera F. J., Watson M. G., 2009, A&A, 500, 749
Elvis M. et al., 2009, ApJ, 184, 158
Elyiv A. et al., 2012, A&A, 537, A131
Fanidakis N., Baugh C. M., Benson A. J., Bower R. G., Cole S., Done C., Frenk C. S., 2011, MNRAS, 410, 53
Fanidakis N. et al., 2012, MNRAS, 419, 2797
Ferrarese L., Ford H., 2005, Space Sci. Rev., 116, 523
Gandhi P. et al., 2006, A&A, 457, 393
Georgakakis A. et al., 2009, MNRAS, 397, 623
Gilli R. et al., 2003, ApJ, 592, 721
Gilli R. et al.2005, A&A, 430, 811 (G05)
Gilli R. et al., 2009, A&A, 494, 33
Gültekin K. et al., 2009, ApJ, 698, 198
Häring N., Rix H.-W., 2004, ApJ, 604, L89
Hickox R. C. et al., 2009, ApJ, 696, 891
Hopkins P. F., Hernquist L., 2006, ApJS, 166, 1
Hopkins P. F., Hernquist L., Cox T. J., Di Matteo T., Robertson B., Springel V., 2005, ApJ, 630, 716
Hopkins P. F., Hernquist L., Cox T. J., Di Matteo T., Robertson B., Springel V., 2006, ApJS, 163, 1
Kaiser N., 1987, MNRAS, 227, 1
Kauffmann G., Heckman T. M., 2009, MNRAS, 397, 135
Kerscher M., Szapudi I., Szalay A. S., 2000, ApJ, 535, L13
Kocevski D. D. et al., 2012, ApJ, 744, 148
Krumpe M., Miyaji T., Coil A. L., 2010, ApJ, 713, 558
Krumpe M., Miyaji T., Coil A., Aceves H., 2012, ApJ, 746, 1
Lagos C. D. P., Cora S. A., Padilla N. D., 2008, MNRAS, 388, 587
Laird E. S. et al., 2009, ApJ, 180, 102
Lehmer B. D. et al., 2005, ApJ, 161, 21

Li C., Kauffmann G., Wang L., White S. D. M., Heckman T. M., Jing Y. P., 2006, MNRAS, 373, 457
Lidz A., Hopkins P. F., Cox T. J., Hernquist L., Robertson B., 2006, ApJ, 641, 41
Limber D. N., 1953, ApJ, 117, 134
Luo B. et al., 2008, ApJ, 179, 19
Luo B. et al., 2010, ApJ, 187, 560
Magorrian J. et al., 1998, AJ, 115, 2285
Marulli F., Bonoli S., Branchini E., Gilli R., Moscardini L., Springel V., 2009, MNRAS, 396, 1404
Miyaji T., Zamorani G., Cappelluti N., Gilli R., Griffiths R. E., Comastri A., Hasinger G., Brusa M., 2007, ApJ, 172, 396
Miyaji T., Krumpe M., Coil A. L., Aceves H., 2011, ApJ, 726, 83
Mo H. J., White S. D. M., 1996, MNRAS, 282, 347
Mo H. J., Jing Y. P., Boerner G., 1992, ApJ, 392, 452
Mountrichas G., Georgakakis A., 2012, MNRAS, 420, 514
Mullis C. R., Henry J. P., Gioia I. M., Böhringer H., Briel U. G., Voges W., Huchra J. P., 2004, ApJ, 617, 192
Myers A. D. et al., 2006, ApJ, 638, 622
Papageorgiou A., Plionis M., Basilakos S., Ragone-Figueroa C., 2012, MNRAS, 422, 106
Peebles P. J. E., 1980, The Large-Scale Structure of the Universe. Princeton Univ. Press, Princeton, NJ
Peebles P. J. E., 1993, Principles of Physical Cosmology, Princeton Univ. Press
Plionis M., Rovilos M., Basilakos S., Georgantopoulos I., Bauer F., 2008, ApJ, 674, L5
Porciani C., Norberg P., 2006, MNRAS, 371, 1824
Press W. H., Schechter P., 1974, ApJ, 187, 425
Puccetti S. et al., 2006, A&A, 457, 501
Ragone-Figueroa C., Plionis M., 2007, MNRAS, 377, 1785
Ross N. P. et al., 2009, ApJ, 697, 1634
Schawinski K., Treister E., Urry C. M., Cardamone C. N., Simmons B., Yi S. K., 2011, ApJ, 727, L31
Shankar F., Weinberg D. H., Miralda-Escudé J., 2009, ApJ, 690, 20
Shen Y. et al., 2009, ApJ, 697, 1656
Sheth R. K., Tormen G., 1999, MNRAS, 308, 119
Silverman J. et al., 2009, in American Astronomical Society Meeting Abstracts Vol. 41 of Bulletin of the American Astronomical Society, Co-evolving Star Formation and AGN Activity within the ZCOSMOS Density Field. p. 511
Silverman J. D. et al., 2010, ApJ, 191, 124
Somerville R. S., Hopkins P. F., Cox T. J., Robertson B. E., Hernquist L., 2008, MNRAS, 391, 481
Starikova S. et al., 2011, ApJ, 741, 15
Tinker J. L., Robertson B. E., Kravtsov A. V., Klypin A., Warren M. S., Yepes G., Gottlöber S., 2010, ApJ, 724, 878
Trouille L., Barger A. J., Cowie L. L., Yang Y., Mushotzky R. F., 2008, ApJ, 179, 1
Valageas P., 2009, A&A, 508, 93
Valageas P., 2011, A&A, 525, A98
Vikhlinin A., Forman W., 1995, ApJ, 455, L109
Virani S. N., Treister E., Urry C. M., Gawiser E., 2006, AJ, 131, 2373
White S. D. M., Frenk C. S., 1991, ApJ, 379, 52
Wolf C., Wisotzki L., Borch A., Dye S., Kleinheinrich M., Meisenheimer K., 2003, A&A, 408, 499
Xue Y. Q. et al., 2011, ApJS, 195, 10
Yang Y., Mushotzky R. F., Barger A. J., Cowie L. L., Sanders D. B., Steffen A. T., 2003, ApJ, 585, L85
Yang Y., Mushotzky R. F., Barger A. J., Cowie L. L., 2006, ApJ, 645, 68

This paper has been typeset from a TEX/LATEX file prepared by the author.